nature COMMUNICATIONS

ARTICLE

Resolving the electromagnetic mechanism of surface-enhanced light scattering at single hot spots

P. Alonso-González[1,*], P. Albella[1,2,*], M. Schnell[1], J. Chen[1,2], F. Huth[1,3], A. García-Etxarri[2,4,5], F. Casanova[1,5], F. Golmar[1,6], L. Arzubiaga[1], L.E. Hueso[1,5], J. Aizpurua[2] & R. Hillenbrand[1,5]

Light scattering at nanoparticles and molecules can be dramatically enhanced in the 'hot spots' of optical antennas, where the incident light is highly concentrated. Although this effect is widely applied in surface-enhanced optical sensing, spectroscopy and microscopy, the underlying electromagnetic mechanism of the signal enhancement is challenging to trace experimentally. Here we study elastically scattered light from an individual object located in the well-defined hot spot of single antennas, as a new approach to resolve the role of the antenna in the scattering process. We provide experimental evidence that the intensity elastically scattered off the object scales with the fourth power of the local field enhancement provided by the antenna, and that the underlying electromagnetic mechanism is identical to the one commonly accepted in surface-enhanced Raman scattering. We also measure the phase shift of the scattered light, which provides a novel and unambiguous fingerprint of surface-enhanced light scattering.

[1] CIC nanoGUNE Consolider, 20018 Donostia-San Sebastián, Spain. [2] Centro de Fisica de Materiales (CSIC-UPV/EHU) and Donostia International Physics Center (DIPC), 20018 Donostia, San Sebastián, Spain. [3] Neaspec GmbH, 82152 Martinsried, Munich, Germany. [4] Department of Materials Science and Engineering, Stanford University, Stanford, California 94305, USA. [5] IKERBASQUE, Basque Foundation for Science, 48011 Bilbao, Spain. [6] I.N.T.I.-CONICET, Av. Gral. Paz 5445, Ed. 42, B1650JKA, San Martín, Bs As, Argentina. *These authors contributed equally to this work. Correspondence and requests for materials should be addressed to R.H. (email: r.hillenbrand@nanogune.eu).

Metal nanostructures can convert incident light into nanoscale confined and strongly enhanced optical fields ('hot spots'), thus acting as the optical analogue of an antenna. When molecules or nanoparticles (objects) are placed at a hot spot, the Raman scattering[1–10], fluorescence[11,12] or infrared absorption[13,14], can be dramatically enhanced. A variety of surface-enhanced Raman scattering (SERS) experiments[15–19] indicate that enormous signal enhancement factors of more than 10^{10} are possible, because the Raman intensity I scales with the fourth power of the local field enhancement f at the metal surface[3,16,20–22], allowing even for single-molecule spectroscopy[4,5,7,23,24]. The direct and quantitative verification of this power law and its underlying electromagnetic scattering mechanism, however, is more than a challenge to tackle. The difficulties arise from the complex processes typically involved in surface-enhanced spectroscopies, where chemical bonding and charge transfer between object and metal nanostructures can occur[12,25–28]. In addition, many experiments rely on measurements of samples exhibiting heterogeneously distributed hot spots of random field enhancement, which forces a statistical evaluation of the enhancement[23].

Here we study the light elastically scattered from an individual object located in the well-defined hot spot of single antennas as a new approach to resolve the role of the antenna in the scattering process. We provide experimental evidence that the scattering off the object is enhanced by the presence of the antenna, and that the underlying electromagnetic mechanism is analogous to that in SERS. Furthermore, the analysis of elastic scattering offers the possibility to access the phase shift induced by the antenna, providing a novel fingerprint of this scattering mechanism.

Results

Electromagnetic mechanism of surface-enhanced scattering. In Figure 1a we illustrate the commonly accepted electromagnetic scattering mechanism in SERS[3,21,28]. An object (O) is located in close proximity to a metal nanostructure. Acting as an antenna (A), the metal nanostructure enhances the incoming field E_{inc} of frequency ω_1 by a factor f_1, generating a local field E_{loc} (hot spot) in its proximity:

$$E_{loc} = f_1 E_{inc} \quad (1)$$

The metal nanostructure also enhances the scattering off the object at the Raman-shifted frequency ω_2 by an enhancement factor f_2. The field E_{AOA} scattered off the object via the antenna is thus given by

$$E_{AOA} \propto f_2 E_{loc} = f_1 f_2 E_{inc} \quad (2)$$

The index AOA indicates the scattering path: the incoming light first polarizes the antenna A, the local field of the antenna polarizes the object O, and finally the local field of the object acts back on the antenna A, which radiates as a result of this interaction. We can approximate $f_1 \approx f_2 \approx f$ when the difference between ω_1 and ω_2 is small and when illumination and detection direction are the same, the latter being a consequence of the reciprocity theorem. In this case, the antenna-enhanced field scattered off the object, E_{AOA}, scales with the square of the local field enhancement[29],

$$E_{AOA} \propto f^2 \quad (3)$$

We note that equation (3) is valid particularly in the case of surface-enhanced elastic scattering, where ω_1 is exactly equal to ω_2. A detailed description of the elastically scattered field E_{AOA} is provided in the Methods section.

It is important to note that for a full analysis of the scattering process we have to consider the complex nature of the field enhancement f:

$$f = |f| e^{i\Delta\varphi_f} \quad (4)$$

Here $|f|$ is the magnitude of the field enhancement and $\Delta\varphi_f$ the phase shift induced by the antenna relative to the incident field. From equations (3) and (4) it is immediately seen that the scattered intensity

$I_{AOA} \propto |E_{AOA}|^2$ (typically measured in an experiment) scales with the fourth power of the magnitude of the local field enhancement,

$$I_{AOA} \propto |f|^4 \quad (5)$$

We also find that there is a phase shift $\Delta\varphi_{AOA}$ between the scattered field $E_{AOA} = |E_{AOA}| e^{i\Delta\varphi_{AOA}}$ and the incident field E_{inc}, which is given by

$$\Delta\varphi_{AOA} = 2\Delta\varphi_f \quad (6)$$

The factor of 2 in equation (6) provides a distinct signature of a surface-enhanced or an antenna-enhanced scattering process. It more clearly reveals the role of the antenna, which is mediating both the illumination of the object as well as the scattering off the object. It is important to note that in SERS we also have to consider chemical enhancement effects and an additional phase shift caused by the Raman process. These effects are not included in equations (1–6) to highlight the electromagnetic mechanism of the enhancement.

Measurement principle and experimental set-up. To access both the magnitude and the phase shift of f, we propose an experimental scheme as illustrated in Figure 1b. We measure the field E_{AOA}, which is elastically backscattered (that is, illumination and detection directions are the same) from an individual object located in the well-defined hot spot of single antennas. Analysing the elastically scattered light ensures that the field enhancements f_1 and f_2 are exactly equal ($f_1 = f_2 = f$), and allows for interferometric measurement of the phase. Furthermore, the object should not be chemically bound to the antenna to exclude chemical effects. In a general detection procedure at frequency ω, however, it is not possible to distinguish between the contributions $E_A(\omega)$ and $E_{AOA}(\omega)$ to the total field $E_T = E_A + E_{AOA}$, where E_A is the field directly scattered by the antenna. To extract $E_{AOA}(\omega)$ from the total field E_T, we modulate sinusoidally the distance d between the antenna and the object at a frequency Ω, according to $d = d_0 + \Delta d \cos(\Omega t)$. Here Δd is the modulation amplitude and d_0 the average antenna–object separation. Such a modulation will not affect the direct scattering contribution $E_A(\omega)$, as it does not depend on the separation distance. However, it will modulate the contribution $E_{AOA}(\omega)$, owing to the nonlinear behaviour of the field enhancement with d, $f = f(d)$. Thus, by demodulating the field E_T at the frequency $n\Omega$ with $n > 1$, we obtain the signal E_n, which is proportional to the field E_{AOA} scattered off the object (for details see the Methods section):

$$E_n \propto E_{AOA} \quad (7)$$

To demonstrate that E_n (and therefore the scattered field E_{AOA}) is proportional to f^2, it is necessary to measure E_n as a function of f. To this end, we measure in the following the signal E_n at the hot spot of
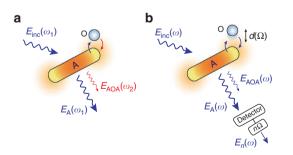

Figure 1 | Schematics of a surface-enhanced light scattering process.
(**a**) Inelastic scattering process ($\omega_1 \neq \omega_2$) from an object (O) in the presence of a metal nanostructure that acts as an optical antenna (A). (**b**) Elastic scattering process ($\omega_1 = \omega_2 = \omega$). $E_{inc}(\omega)$ denotes the incident field, $E_A(\omega)$ is the field directly radiated by the antenna, and $E_{AOA}(\omega)$ is the field radiated by the object via the antenna. To select E_{AOA}, the antenna–object distance d is modulated at frequency Ω, and the detector signal is demodulated at the higher harmonic frequency $n\Omega$.

different well-defined antennas and relate it to the calculated local field enhancement f.

We note that equation (3) (and subsequently equation (7)) is valid for strong field enhancements $f \gg 1$ and does not account for the vectorial nature of the fields[30]. However, a more rigorous and general tensorial formulation (see derivation of E_{AOA} in the Methods section) proves that equation (3) indeed applies for scattering configura-tions where the object of interest is located at individual hot spots of optical antennas, as is the case in the following experiments.

We experimentally realize the scheme proposed in Figure 1b with the use of a scattering-type scanning near-field optical microscope (s-SNOM, Fig. 2)[31,32]. As schematically illustrated in Figure 3a, the apex of the vertically oscillating Si tip mimics the object (O), while the metal rod acts as an antenna (A) that converts the incident infra-red radiation of a wavelength $\lambda = 11.1\,\mu m$ (with polarization parallel to the rod) into strongly concentrated fields at the rod extremities (hot spots)[31]. The horizontally polarized light backscattered from the tip-antenna configuration is detected with a pseudo-heterodyne Michelson interferometer[33] (Fig. 2). Demodulation of the detector signal at $n\Omega$ yields the amplitude $|E_n|$ and phase shift $\Delta\varphi_n$. To iden-tify the hot spots, we scan the tip across the antenna and record the sample height, as well as amplitude $|E_n|$ and phase $\Delta\varphi_n$ as a function of the tip position (Fig. 3b). In the amplitude map we observe the strongest signals $|E_n|$ at the rod extremities, which experimentally proves the existence of two hot spots on the metal rod. The phase map shows that the signal $\Delta\varphi_n$ is nearly constant across the antenna.

Analogous to classical radio wave antennas, the resonance and thus highest field enhancement for Au rods is expected at a length $L_{res} = \lambda_{eff}/2$, where λ_{eff} is the effective wavelength[34,35]. By changing the antenna length L at a fixed wavelength, we can thus precisely control the field enhancement f at the rod extremities, which is the key to establish a quantitative dependence between the local field enhancement f and the scattered field E_n. We thus study in the fol-lowing an antenna array where the antenna length decreases from the top to the bottom and from the left to the right (for antenna fab-rication details see Methods section). In Figure 3c we show topog-raphy, amplitude $|E_n|$ and phase $\Delta\varphi_n$ maps of this antenna array, while in Figure 4a we show zoom-in images of selected antennas. We observe that with increasing antenna lengths L, the amplitude signal increases until it reaches a maximum value at a rod length of about $L = 3.7\,\mu m$, consistent with the theoretical antenna resonance. With further increasing length, the amplitude decreases. This obser-vation clearly reveals the resonance behaviour of the antennas[36]. The simultaneously acquired phase maps reveal a continuously increas-ing phase with increasing rod length, providing further evidence that we trace a resonance[37].
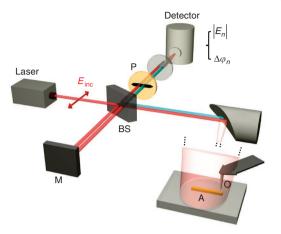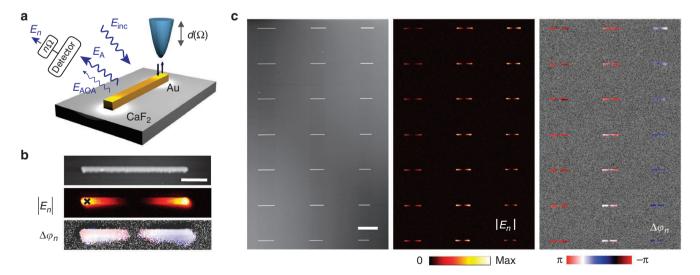

Figure 2 | Set-up for verifying surface-enhanced elastic light scattering. The set-up comprises a scattering-type scanning near-field optical microscope (s-SNOM, from Neaspec GmbH), which is based on an atomic force microscope (AFM). The apex of a conventional Si tip acts as the scattering object (O). The antenna and tip are illuminated at an angle of about 50° relative to the surface normal with the focused beam of a CO_2 laser operating at 11.1 μm. The polarization of the illuminating beam E_{inc} is parallel to the long axis of the metal rod (s-polarized light). The field backscattered by the antenna (A) and the tip (O) is collected and detected with a pseudo-heterodyne interferometer (M denotes the reference mirror and BS the beamsplitter). The polarizer P ensures that s-polarized light is detected. To obtain a modulation of the distance between tip and antenna, the tip is oscillating vertically at a frequency $\Omega \approx 300\,KHz$ and with an amplitude of 70 nm. Demodulation of the detector signal at a higher harmonic $n\Omega$ yields the amplitude and phase signals $|E_n|$ and $\Delta\varphi_n$.

Figure 3 | Spatial mapping of surface-enhanced light scattering. (a) A Si tip (vertically oscillating at frequency Ω) is scanned across a Au rod antenna (A). Both antenna and tip (the latter mimicking the scattering object O) are illuminated with s-polarized light. The s-polarized light backscattered from the tip-antenna configuration is detected interferometrically (not shown). Demodulation of the detector signal at a higher harmonic $n\Omega$ yields the amplitude $|E_n|$ and the phase $\Delta\varphi_n$ at each position of the tip. **(b)** Topography, amplitude $|E_n|$ and phase shift $\Delta\varphi_n$ maps of a Au rod antenna. The scale bar denotes 1 μm. **(c)** From left to right, topography, amplitude $|E_n|$ and phase shift $\Delta\varphi_n$ maps of Au rods. The length of the rods decreases from the top to the bottom and from the left to the right). The illumination wavelength was 11.1 μm. Demodulation was done with $n = 4$. The scale bar denotes 5 μm.
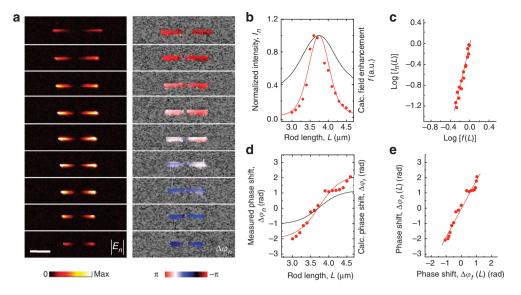
Figure 4 | Verification of antenna-mediated elastic light scattering. (**a**) Amplitude $|E_n|$ and phase shift $\Delta\varphi_n$ maps of Au rods of different lengths. All the maps were recorded at an illumination wavelength of 11.1 μm. Demodulation was done with $n = 4$. The scale bar denotes 2 μm. (**b**) Measured intensity $I_n \propto |E_n|^2$ (red symbols) and calculated field enhancement f (black solid line) at the hot spot (marked by a cross in Fig. 3b) as a function of the antenna length L. Both quantities are normalized to their maximum value. The red solid line shows the function $f^{4.08}$ (L). (**c**) Parametric representation of $\log[I_n(L)]$ and $\log[f(L)]$ (red symbols). A linear least-square fitting of the data points (red solid line) yields a slope of 4.08. (**d**) Measured phase shift $\Delta\varphi_n$ (red symbols) and calculated phase shift $\Delta\varphi_f$ (black solid line) at the hot spot (marked by a cross in Fig. 3b) as a function of antenna length L. The red solid line shows the function 1.85 $\Delta\varphi_f$ (L). (**e**) Parametric representation of $\Delta\varphi_n(L)$ and $\Delta\varphi_f(L)$ (red symbols). Linear least-square fitting of the data yields the relation $\Delta\varphi_n = 1.85\Delta\varphi_f$.

To relate the scattered field E_n with the local field enhancement f, we measure amplitude $|E_n|$ and phase $\Delta\varphi_n$ at the hot spot (marked by a cross in Fig. 3b) as a function of the antenna length L and compare them to the numerically calculated magnitude $|f|$ and phase $\Delta\varphi_f$ of the local field enhancement. The calculations of the magnitude and phase at the hot spots were performed with the use of a finite-difference time-domain (FDTD) method (Lumerical FDTD Solutions). The same wavelength and geometrical antenna parameters as in the experiment were used. The dielectric values for Au and the refractive index of the CaF$_2$ substrate, $n_{CaF_2} \cong 1.26 + 0.005i$, were taken from Palik[38].

Relating scattered intensity and local field enhancement. Figure 4b displays the measured intensity $I_n \propto |E_n|^2$ (red symbols) and the calculated field enhancement f (black solid line) at the hot spots indicated by the cross in Figure 3b, both normalized to their maximum value. We clearly see the resonance behaviour, with the resonance appearing at $L = 3.7$ μm for both I_n and f. In Figure 4c we show a parametric representation of $\log[I_n(L)]$ and $\log[f(L)]$ (red symbols). We find a linear behaviour, revealing that the scattered intensity I_n and the field enhancement f are related by a power law. Linear least-square fitting of the data points yields a slope of 4.08. By plotting $f^{4.08}(L)$ in Figure 4b (red solid line), we find a good agreement with the measured intensity $I_n(L)$. Our results clearly verify that the intensity scattered from a nanoscale object located in a hot spot scales with the fourth power of the local field enhancement, $I \propto f^4$. The slight quantitative discrepancy between the experimental and theoretical exponent can be attributed to uncertainties in the antenna fabrication process and dielectric values, which have a particularly strong impact in establishing a large-exponent power law.

Figure 4d displays the measured phase shift $\Delta\varphi_n$ (red symbols) and the calculated phase shift $\Delta\varphi_f$ (black solid line) as a function of the antenna length L. As expected, both of them increase continuously with the antenna length L (ref. 37). In Figure 4e we show a parametric representation of $\Delta\varphi_n(L)$ and $\Delta\varphi_f(L)$ (red symbols). Linear least-square fitting of the data yields a slope of 1.85. By plotting $\Delta\varphi_f(L)$ multiplied by the factor 1.85 in Figure 4d (red solid

line), we find an excellent agreement with the measured phase shift $\Delta\varphi_n(L)$. This factor (yielding the difference between the measured phase shift and the phase shift induced by the antenna) is close to the expected value of 2 (as predicted in equation (6)), thus clearly proving the double role of the antenna, which is both illuminating the object as well as scattering off the object.

Antenna-enhanced light scattering is particularly efficient when the objects of interest are located in nanoscale antenna gaps, where the local field enhancement reaches maximum values[8]. To study the scattering mechanism in this case, we recorded the field scattered from the Si tip in the proximity of infrared gap antennas (Fig. 5a). The amplitude and phase maps of the resonant antenna are shown in Figure 5b and c, clearly visualizing the hot spot in the antenna gap. Owing to the capacitive coupling across the gap[31], this hot spot exhibits a much stronger field enhancement and field confinement compared with that observed in single rods (Fig. 3b). From a zoom-in image (Fig. 5b), we measure for the hot spot a full width at half maximum of about 50 nm. Following an identical procedure as the one applied in Figure 4, we establish the relation between the field scattered from the tip and the local field enhancement exactly at the gap centre. To this end, we mapped gap antennas with a fixed gap and varying arm length L, and measured the field $|E_n|$ and the phase shift $\Delta\varphi_n$ at the gap centre as a function of L. We also calculated the magnitude $|f|$ and phase $\Delta\varphi_f$ of the field enhancement at the gap centre. From a parametric representation of $\log[I_n(L)]$ and $\log[f(L)]$ (Fig. 5d), we again find that the intensity scattered by the tip scales with nearly the fourth power of the field enhancement. The difference between the exponent of 4.56 determined from our study and the expected value of 4 can be assigned to uncertainties in the antenna fabrication process, yielding variations in the antenna dimensions (for example, length, width and gap size) with respect to the design values used for the near-field calculations. Particularly difficult to reproduce by electron-beam lithography on the insulating CaF$_2$ substrate is the gap, which is precisely where the local field enhancement in Figure 5d is evaluated. In Figure 5e we show a parametric plot of $\Delta\varphi_n(L)$ and $\Delta\varphi_f(L)$, yielding clear evidence that the phase shift of the scattered field E_{AOA} is twice the phase shift of the local field at the hot
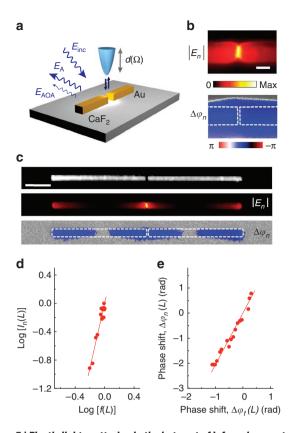
Figure 5 | Elastic light scattering in the hot spot of infrared gap antennas.
(**a**) A Si tip (vertically oscillating at frequency Ω) is scanned across a
Au rod antenna (A). Both antenna and tip (the latter mimicking the
scattering object O) are illuminated with s-polarized light. The s-polarized
light backscattered from the tip-antenna configuration is detected
interferometrically (not shown). Demodulation of the detector signal
at $n\Omega$ yields the amplitude $|E_n|$ and phase shift $\Delta\varphi_n$ at each position of
the tip. (**b**) Zoom-in amplitude $|E_n|$ and phase shift $\Delta\varphi_n$ images of the
gap region in a resonant gap antenna. A full width at half maximum of the
hot spot of about 50 nm is measured. The scale bar denotes 100 nm.
(**c**) Topography, amplitude $|E_n|$ and phase shift $\Delta\varphi_n$ maps of a resonant gap
antenna. The maps were recorded at an excitation wavelength of 11.1 μm
and demodulation was done with $n = 4$. The scale bar denotes 2 μm.
(**d**) Parametric representation of $\log[I_n(L)]$ and $\log[f(L)]$ (red symbols).
A linear least-square fitting of the data points (red solid line) yields a slope
of 4.56. (**e**) Parametric representation of $\Delta\varphi_n(L)$ and $\Delta\varphi_f(L)$ (red symbols).
Linear least-square fitting of the data yields the relation $\Delta\varphi_n = 1.99\Delta\varphi_f$.

spot ($\Delta\varphi_n(L) = 1.99\Delta\varphi_f(L)$). These observations confirm the results
obtained with single rods (Fig. 4) and thus corroborate the electro-
magnetic mechanism in antenna-enhanced light scattering.

Discussion

Our findings might have particular implications in surface-
enhanced infrared absorption (SEIRA) spectroscopy, where objects
adsorbed on rough metal films or antennas exhibit an enhanced
infrared fingerprint spectrum. SEIRA—actually yielding extinction
spectra—is typically assigned to an enhanced infrared absorption
of the objects. The enhanced infrared scattering from the objects is
barely considered. However, the scattering from the object might be
a significant contribution to the extinction, as it scales with f^4, while
the infrared absorption scales only with f^2. Future interpretation
of SEIRA thus might need to consider also the scattering process.
On the other hand, the strongly enhanced scattering cross-section
might be applied for the development of surface-enhanced infrared
scattering spectroscopy.

In conclusion, our results provide a rigorous verification of the
widely accepted electromagnetic enhancement mechanism in sur-
face- and antenna-enhanced spectroscopy, more than 30 years after
it was proposed to explain the electromagnetic contribution in SERS.
We also establish that the enhancement mechanism for elastic and
inelastic (Raman) scattering is the same, and thus generalize the elec-
tromagnetic mechanism of SERS. Furthermore, the verification of the
phase shift involved in the elastic scattering process introduces a new
paradigm to characterize and manipulate surface-enhanced coherent
scattering processes, which might be of fundamental and technologi-
cal importance in optical information and sensing applications.

Methods

Derivation of E_{AOA}. In the following we show that the elastic light scattering from
an object at the hot spot of an optical antenna, E_{AOA}, scales with the fourth power
of the local field enhancement. We consider a general elastic light scattering proc-
ess similar to the one shown in Figure 1b, where incoming and scattered radiations
occur at frequency ω. Both antenna (A) and object (O) are characterized by means
of their corresponding polarizabilities α_A and α_O, with $\alpha_A \gg \alpha_O$. When an incident
field $E_{inc}(\omega)$ impinges on the antenna and object, a multiple scattering process
occurs. The resulting total scattered field $E_T(\omega)$ can be expressed as a coherent sum
of the contribution of the different scattering orders as:

$$E_T(\omega) = E_A(\omega) + E_O(\omega) + E_{AO}(\omega) + E_{OA}(\omega) + E_{AOA}(\omega) + \dots \quad (8)$$

From now on, an implicit ω dependence will be assumed in all of the expressions.
In equation (8) the term

$$E_A = G_A \alpha_A E_{inc} \quad (9)$$

is the field radiated directly by the antenna with $G_A = G_A(r \to \infty)$ being the cor-
responding Green's function evaluated in the far field, for example, at a distant
detector. The term

$$E_O = G_O \alpha_O E_{inc} \quad (10)$$

is the field radiated directly by the object, where $G_O = G_O(r \to \infty)$ is the Green's
function describing the scattering from the object. The term

$$E_{OA} = G_O \alpha_O f E_{inc} \quad (11)$$

is the field radiated directly by the object after being illuminated by the local field
$E_{loc} = f E_{inc}$ produced by the antenna. The term

$$E_{AO} = G_A f \alpha_O E_{inc} \quad (12)$$

is the field scattered from the object via the antenna. The term

$$E_{AOA} = G_A f \alpha_O f E_{inc} \quad (13)$$

describes the field scattered from the object via the antenna, after being illuminated
by the local field produced by the antenna. The direct scattering off the object E_O
in equation (8) can be neglected because the polarizability of the object α_O is, by
definition, smaller than the polarizability of the antenna α_A. Thus, E_O is negligible
when compared with E_A. We also note that the exact total radiation in equation
(8) should include all the successive interaction events in the scattering process.
Nevertheless, the small value of α_O allows for a truncation of E_T at the first order
of α_O, that is, after the term E_{AOA}, as shown in equation (8). Moreover, if the field
enhancement is large ($f \gg 1$), as it is the case in a hot spot of an antenna, the con-
tributions E_{OA} and E_{AO} (which scale linearly with f) to E_T are much smaller than
E_{AOA} (which scales with the square of f). The total radiated field E_T (equation (8))
can be thus reduced to:

$$E_T \approx E_A + E_{AOA} \quad (14)$$

The field E_{AOA} in equation (13), which is the one studied in this communication,
can be evaluated considering the tensorial nature of the polarizability $\boldsymbol{\alpha}_O$ (diagonal
tensor of components $\alpha_{O,ii}$ with $i = x, y, z$) and the field enhancement $\mathbf{f}$ (tensor
of components f_{ij} with $i, j = x, y, z$). With an incident field $E_{inc,x}$ polarized in the
x-direction (defined here to be parallel to the long axis of the antenna, as in our
experimental situation) we obtain:

$$E_{AOA,x} = \mathbf{G}_A \begin{pmatrix} \alpha_{O,xx} f_{xx} f_{xx} E_{inc,x} + \alpha_{O,yy} f_{yx} f_{yx} E_{inc,x} + \alpha_{O,zz} f_{zx} f_{zx} E_{inc,x} \\ 0 \\ 0 \end{pmatrix} \quad (15)$$

where f_{ij} is the field enhancement factor of the i-component induced by the
j-component of the incident field $E_{inc,j}$.

In the case of an isotropic polarizability of the object, $\alpha_{O,xx} = \alpha_{O,yy} = \alpha_{O,zz}$, equation (15) yields the well-known scalar power law $E_{AOA,x} \propto [(f_{xx})^2 + (f_{yx})^2 + (f_{zx})^2] = f^2$ as described by equation (13). In case of an anisotropic object (as the tip in our experiment), the general solution of $E_{AOA,x}$ (equation (15)) prevails. However, at the extremity of single dipolar antennas and at the gap between two coupled antennas (the two situations considered in this communication), one component of the enhancement dominates over the others. $f_{xx} \gg f_{yx}, f_{zx}$ in the gap of a coupled antenna and $f_{zx} \gg f_{xx}, f_{yx}$ on top of the single antenna extremities. In these cases, we can consider $f \approx f_{xx}$ or $f \approx f_{zx}$, respectively, and $E_{AOA,x}$ can be expressed as

$$E_{AOA,x}(\omega) \approx G_A f_{xx} \alpha_{O,xx} f_{xx} E_{inc,x} \propto f^2 \qquad (16)$$

at the antenna gap, or

$$E_{AOA,x}(\omega) \approx G_A f_{zx} \alpha_{O,zz} f_{zx} E_{inc,x} \propto f^2 \qquad (17)$$

on the extremity of an isolated antenna. Equations (16) and are identical to the scalar description (equation (13)) of surface-enhanced light scattering.

Mathematical relationship between E_n and E_{AOA}. In the following we analyse the dependence of the n-th order demodulated detector signal $E_n(\omega)$ on the field-enhancement factor. $E_n(\omega)$ is obtained as the n-th order coefficient of the Fourier transform:

$$E_n(\omega) \propto \int E_T(\omega)\, e^{-in\Omega t}\mathrm{d}t = \int (E_A(\omega) + E_{AOA}(\omega))\, e^{-in\Omega t}\mathrm{d}t$$
$$= \int E_{AOA}(\omega)e^{-in\Omega t}\mathrm{d}t \qquad (18)$$

Substituting $E_{AOA}(\omega)$ according to equation (13), we obtain:

$$E_n(\omega) \propto \int G_A \alpha_O E_{inc}(\omega) \cdot f(d) \cdot f(d) \cdot e^{-in\Omega t}\mathrm{d}t$$
$$= G_A \alpha_O E_{inc}(\omega)\int f(d) \cdot f(d) \cdot e^{-in\Omega t}\mathrm{d}t \qquad (19)$$

Normalizing the integral in equation (19) by $f = f_0 = f(d_0)$, we find:

$$E_n(\omega) = G_A \alpha_O E_{inc}(\omega)\, f_0^2 \int (f(d)/f_0)^2\, e^{-in\Omega t}\mathrm{d}t \qquad (20)$$

By defining the normalized n-th Fourier coefficient $\xi_n(d_0)$ as

$$\xi_n(d_0) = \int (f(d)/f_0)^2\, e^{-in\Omega t}\mathrm{d}t \qquad (21)$$

we can express $E_n(\omega)$ in terms of f_0 and $\xi_n(d_0)$ as

$$E_n(\omega) = G_A \alpha_O E_{inc}(\omega)f_0^2\xi_n(d_0) = E_{AOA}(\omega)\xi_n(d_0) \qquad (22)$$

In Supplementary Figure S1 we show that for linear dipole antennas $\xi_n(d_0)$ is independent of the antenna length. Thus, in equation (22), $\xi_n(d_0)$ can be taken as a constant for every single antenna at a particular distance d_0, yielding

$$E_n(\omega) \propto E_{AOA}(\omega) \propto f^2 \qquad (23)$$

Antenna fabrication. We fabricated Au rods with a nominal length L between 2 and 5 μm and a fixed width of 100 nm on a double-side–polished CaF$_2$ (100) substrate by high-resolution electron-beam lithography. A bilayer polymethyl methacrylate (with 495,000 molecular weight at the bottom and 950,000 molecular weight at the top) was used as electron-sensitive polymer. The Au film with a thickness of 40 nm was thermally evaporated in high vacuum on top of a 3-nm thick Ti layer, electron-beam evaporated for adhesion purposes. A lift-off process yields the Au nanorods.

References

1. Fleischmann, M., Hendra, P. J & McQuillan, A. J. Raman spectra of pyridine adsorbed at a silver electrode. *Chem. Phys. Lett.* **26,** 163–166 (1974).
2. Jeanmaire, D. L. & Van Duyne, R. P. Surface raman spectroelectrochemistry: Part I. Heterocyclic, aromatic, and aliphatic amines adsorbed on the anodized silver electrode. *J. Electroanal. Chem. Interfacial Electrochem.* **84,** 1–20 (1977).
3. Moskovits, M. Surface-enhanced spectroscopy. *Rev. Mod. Phys.* **57,** 783 (1985).
4. Kneipp, K. *et al.* Single molecule detection using surface-enhanced raman scattering (SERS). *Phys. Rev. Lett.* **78,** 1667 (1997).
5. Nie, S. & Emory, S. R. Probing single molecules and single nanoparticles by surface-enhanced raman scattering. *Science* **275,** 1102–1106 (1997).
6. Campion, A. & Kambhampati, P. Surface-enhanced Raman scattering. *Chem. Soc. Rev.* **27,** 241–250 (1998).
7. Xu, H., Bjerneld, E. J., Käll, M. & Börjesson, L. Spectroscopy of single hemoglobin molecules by surface enhanced Raman scattering. *Phys. Rev. Lett.* **83,** 4357–4360 (1999).
8. Xu, H., Aizpurua, J., Kall, M. & Apell, P. Electromagnetic contributions to single-molecule sensitivity in surface-enhanced Raman scattering. *Phys. Rev. E* **62,** 4318 (2000).
9. Moskovits, M. Surface-enhanced Raman spectroscopy: a brief retrospective. *J. Raman Spectrosc.* **36,** 485–496 (2005).
10. Li, Z., Shegai, T., Haran, G. & Xu, H. Multiple-particle nanoantennas for enormous enhancement and polarization control of light emission. *ACS Nano* **3,** 637–642 (2009).
11. Kühn, S., Hakanson, U., Rogobete, L. & Sandoghdar, V. Enhancement of single-molecule fluorescence using a gold nanoparticle as an optical nanoantenna. *Phys. Rev. Lett.* **97,** 017402 (2006).
12. Anger, P., Bharadwaj, P. & Novotny, L. Enhancement and quenching of single-molecule fluorescence. *Phys. Rev. Lett.* **96,** 113002 (2006).
13. Neubrech, F. *et al.* Resonant plasmonic and vibrational coupling in a tailored nanoantenna for infrared detection. *Phys. Rev. Lett.* **101,** 157403 (2008).
14. Osawa, M. Dynamic processes in electrochemical reactions studied by surface-enhanced infrared absorption spectroscopy (SEIRAS). *Bull. Chem. Soc. Jpn* **70,** 2861–2880 (1997).
15. Lee, S. J., Guan, Z., Xu, H. & Moskovits, M. Surface-enhanced Raman spectroscopy and nanogeometry: the plasmonic origin of SERS. *J. Phys. Chem. C* **111,** 17985–17988 (2007).
16. Le Ru, E. C. *et al.* Experimental verification of the SERS electromagnetic model beyond the |E|^4 approximation: polarization effects. *J. Phys. Chem. C* **112,** 8117–8121 (2008).
17. McFarland, A. D., Young, M. A., Dieringer, J. A. & Van Duyne, R. P. Wavelength-scanned surface-enhanced Raman excitation spectroscopy. *J. Phys. Chem. B* **109,** 11279–11285 (2005).
18. Lal, S., Grady, N. K., Goodrich, G. P. & Halas, N. J. Profiling the near field of a plasmonic nanoparticle with Raman-based molecular rulers. *Nano Lett.* **6,** 2338–2343 (2006).
19. Doherty, M. D., Murphy, A., McPhillips, J., Pollard, R. J. & Dawson, P. Wavelength dependence of Raman enhancement from gold nanorod arrays: quantitative experiment and modeling of a hot spot dominated system. *J. Phys. Chem. C* **114,** 19913–19919 (2010).
20. Chalmers, J. M. & Griffiths, P. R. *Handbook of Vibrational Spectroscopy* (John Wiley, 2002).
21. Le Ru, E. C. & Etchegoin, P. G. Rigorous justification of the E4 enhancement factor in surface enhanced Raman spectroscopy. *Chem. Phys. Lett.* **423,** 63–66 (2006).
22. Fazio, B. *et al.* Re-radiation enhancement in polarized surface-enhanced resonant Raman scattering of randomly oriented molecules on self-organized gold nanowires. *ACS Nano* **5,** 5945–5956 (2011).
23. Le Ru, E. C., Etchegoin, P. G. & Meyer, M. Enhancement factor distribution around a single surface-enhanced Raman scattering hot spot and its relation to single molecule detection. *J. Chem. Phys.* **125,** 204701–204713 (2006).
24. Camden, J. P. *et al.* Probing the structure of single-molecule surface-enhanced Raman scattering hot spots. *J. Am. Chem. Soc.* **130,** 12616–12617 (2008).
25. Fromm, D. P. *et al.* Exploring the chemical enhancement for surface-enhanced Raman scattering with Au bowtie nanoantennas. *J. Chem. Phys.* **124,** 061101–061104 (2006).
26. Saikin, S. K., Chu, Y., Rappoport, D., Crozier, K. B. & Aspuru-Guzik, A. Separation of electromagnetic and chemical contributions to surface-enhanced Raman spectra on nanoengineered plasmonic substrates. *J. Phys. Chem. Lett.* **1,** 2740–2746 (2010).
27. Yoshida, K.-i. *et al.* Quantitative evaluation of electromagnetic enhancement in surface-enhanced resonance Raman scattering from plasmonic properties and morphologies of individual Ag nanostructures. *Phys. Rev. B* **81,** 115406 (2010).
28. Xu, H. *et al.* Unified treatment of fluorescence and Raman scattering processes near metal surfaces. *Phys. Rev. Lett.* **93,** 243002 (2004).
29. Novotny, L. & Hecht, B. *Principles of Nano-Optics* (Cambridge University Press, 2006).
30. Deutsch, B., Hillenbrand, R. & Novotny, L. Visualizing the optical interaction tensor of a gold nanoparticle pair. *Nano Lett.* **10,** 652–656 (2010).
31. Schnell, M. *et al.* Controlling the near-field oscillations of loaded plasmonic nanoantennas. *Nat. Photon.* **3,** 287–291 (2009).
32. Schnell, M., Garcia-Etxarri, A., Alkorta, J., Aizpurua, J. & Hillenbrand, R. Phase-resolved mapping of the near-field vector and polarization state in nanoscale antenna gaps. *Nano Lett.* **10,** 3524–3528 (2010).
33. Ocelic, N., Huber, A. & Hillenbrand, R. Pseudoheterodyne detection for background-free near-field spectroscopy. *Appl. Phys. Lett.* **89,** 101124–101123 (2006).
34. Novotny, L. Effective wavelength scaling for optical antennas. *Phys. Rev. Lett.* **98,** 266802 (2007).
35. Bryant, G. W., Garcia de Abajo, F. J. & Aizpurua, J. Mapping the plasmon resonances of metallic nanoantennas. *Nano Lett.* **8,** 631–636 (2008).
36. Dorfmüller, J. *et al.* Fabry-Pérot resonances in one-dimensional plasmonic nanostructures. *Nano Lett.* **9,** 2372–2377 (2009).
37. Biagioni, P. *et al.* Near-field polarization shaping by a near-resonant plasmonic cross antenna. *Phys. Rev. B* **80,** 153409 (2009).
38. Palik, E. D. *Handbook of Optical Constants of Solids* (Academic Press, 1985).

Author contributions

P.A.-G. and R.H. designed the experiments. F.H. and P.A.-G. set up the near-field microscope. F.C., F.G., L.A. and L.E.H. contributed to sample preparation. P.A.-G. performed the experiments with the help of J.C. P.A.-G., P.A., J.A., and R.H. analysed and discussed the data. P.A., and J.A. performed the calculations and together with R.H. and A.G.-E. established the theoretical framework. M.S. contributed to the discussion and interpretation of the results. R.H. wrote the manuscript together with J.A., P.A.-G. and P.A.

Additional information

Supplementary Information accompanies this paper at http://www.nature.com/naturecommunications

Competing financial interests: P.A.-G, P.A., M.S, J.C., F.H., A.G.-E., F.C., F.G., L.A., L.E.H. and J.A. declare no competing financial interests. R.H. is co-founder of Neaspec GmbH, a company producing scattering-type scanning near-field optical microscope systems, such as the one used in this study.

Reprints and permission information is available online at http://npg.nature.com/reprintsandpermissions/

How to cite this article: Alonso-González, P. *et al.* Resolving the electromagnetic mechanism of surface-enhanced light scattering at single hot spots. *Nat. Commun.* 3:684 doi: 10.1038/ncomms1674 (2012).